








ARTICLE

DOI: 10.1038/s41467-018-04845-x

OPEN

Carbon nitride supported Fe₂ cluster catalysts with superior performance for alkene epoxidation

Shubo Tian¹, Qiang Fu ^{2,3}, Wenxing Chen ^{1,4}, Quanchen Feng¹, Zheng Chen¹, Jian Zhang ¹,
Weng-Chon Cheong¹, Rong Yu ⁵, Lin Gu⁶, Juncai Dong ⁷, Jun Luo ⁸, Chen Chen¹, Qing Peng¹,
Claudia Draxl², Dingsheng Wang ¹ & Yadong Li¹

Sub-nano metal clusters often exhibit unique and unexpected properties, which make them particularly attractive as catalysts. Herein, we report a “precursor-preselected” wet-chemistry strategy to synthesize highly dispersed Fe₂ clusters that are supported on mesoporous carbon nitride (mpg-C₃N₄). The obtained Fe₂/mpg-C₃N₄ sample exhibits superior catalytic performance for the epoxidation of *trans*-stilbene to *trans*-stilbene oxide, showing outstanding selectivity of 93% at high conversion of 91%. Molecular oxygen is the only oxidant and no aldehyde is used as co-reagent. Under the same condition, by contrast, iron porphyrin, single-atom Fe, and small Fe nanoparticles (ca. 3 nm) are nearly reactively inert. First-principles calculations reveal that the unique reactivity of the Fe₂ clusters originates from the formation of active oxygen species. The general applicability of the synthesis approach is further demonstrated by producing other diatomic clusters like Pd₂ and Ir₂, which lays the foundation for discovering diatomic cluster catalysts.

¹Department of Chemistry, Tsinghua University, 100084 Beijing, China. ²Institut für Physik and IRIS Adlershof, Humboldt-Universität zu Berlin, 12489 Berlin, Germany. ³School of Chemistry and Chemical Engineering, Shandong University, 250100 Jinan, China. ⁴Beijing Key Laboratory of Construction Tailorable Advanced Functional Materials and Green Applications, School of Materials Science and Engineering, Beijing Institute of Technology, 100081 Beijing, China. ⁵Beijing National Center for Electron Microscopy, School of Materials Science and Engineering, Tsinghua University, 100084 Beijing, China. ⁶Institute of Physics, Chinese Academy of Sciences, 100190 Beijing, China. ⁷Beijing Synchrotron Radiation Facility, Institute of High Energy Physics, Chinese Academy of Sciences, 100049 Beijing, China. ⁸Center for Electron Microscopy, Tianjin University of Technology, 300384 Tianjin, China. These authors contributed equally: Shubo Tian, Qiang Fu, Wenxing Chen. Correspondence and requests for materials should be addressed to D.W. (email: wangdingsheng@mail.tsinghua.edu.cn)

Metal cluster catalysts at the sub-nanoscale often possess unique and unexpected catalytic properties that normally do not exist in the corresponding nanoparticle counterparts^{1–9}. Upon deposition on a substrate, the few atoms in the catalysts could provide a compelling platform for bridging heterogeneous and homogeneous catalysis^{10–16}. Since the nature of sub-nano systems can be significantly altered by adding or removing just one atom, gaining a deep understanding on the structure–property correlations is of great importance for designing catalysts with extraordinary activity and selectivity^{17–19}. While the structures and compositions of sub-nano clusters can be well characterized by X-ray absorption fine structure (XAFS) spectra in conjunction with high-resolution electron microscopes^{16,20,21}, synthesizing monodispersed metal catalysts with atomic precision, which is the prime prerequisite, remains a great challenge.

Epoxides constitute important intermediates in fine chemical industry and biotransformation. In current processes for alkene epoxidation in liquids, an extensive use of expensive oxidants or large doses of co-reagents is usually required^{22–24}, which inevitably leads to an increase in the costs. To overcome this drawback, several homogeneous catalysts like iron- and ruthenium-substituted polyoxometalates have been developed, allowing O₂ to be the oxidant without a need for any co-reductant^{25,26}. In contrast, corresponding heterogeneous catalysts are rarely reported. Supported sub-nano metal clusters, via bridging both types of catalysts, are thus expected to play a role in the reactions.

Herein, we employ a “precursor-preselected” wet-chemistry strategy to prepare Fe₂ clusters dispersed on an mpg-C₃N₄ substrate. The preselected metal precursors ensure the formation of diatomic clusters, whereas mpg-C₃N₄ provides abundant anchoring sites to stabilize the metallic species. The pyrolysis process is carefully optimized to guarantee a complete removal of organic ligands from the precursors, and at the same time,

prevent agglomeration of the Fe₂ clusters. The prepared Fe₂/mpg-C₃N₄ sample exhibits excellent catalytic performance toward epoxidation of *trans*-stilbene, which is absent when using iron porphyrin, single-atom Fe, or small Fe nanoparticles as the catalyst. First-principles calculations reveal that the unique reactivity of the Fe₂ clusters is attributed to the formation of active oxygen species. The synthesis approach reported in this work can be applied to produce other transition-metal dimers and paves the way for a precise design of nanocatalysts at the atomic scale.

Results

Synthesis and characterization of Fe₂/mpg-C₃N₄ samples. Mesoporous graphitic carbon nitride was prepared following the previous literature²⁷. The transmission electron microscopy (TEM) image (Supplementary Figure 1) and the X-ray diffraction (XRD) pattern (Supplementary Figure 2) demonstrate a graphitic packing structure of mpg-C₃N₄ with disordered spherical pores²⁷. The infrared (IR) spectrum (Supplementary Figure 3) evidences the formation of extended C–N–C networks, according to the typical C–N heterocycle stretching modes in the region of ca. 1100–1600 cm^{−1} and the breathing mode of tri-s-triazine units at about 810 cm^{−1}^{28,29}. Regarding the produced Fe₂/mpg-C₃N₄ samples, there is no IR absorption peak that corresponds to the organic molecules in the Fe₂ precursor, indicating a complete removal of the ligands. The content of Fe is estimated to be about 0.15 wt% according to the inductively coupled plasma optical emission spectrometry (ICP-OES) analysis. Upon deposition of the Fe₂ clusters, the XRD pattern does not show any additional diffraction peaks of Fe (Supplementary Figure 2), and there are no obvious Fe particles in the TEM image (Supplementary Figure 4). These results serve as the first indication that Fe₂ clusters do not agglomerate during the pyrolysis process. The homogeneous distribution of the diatomic clusters is further supported

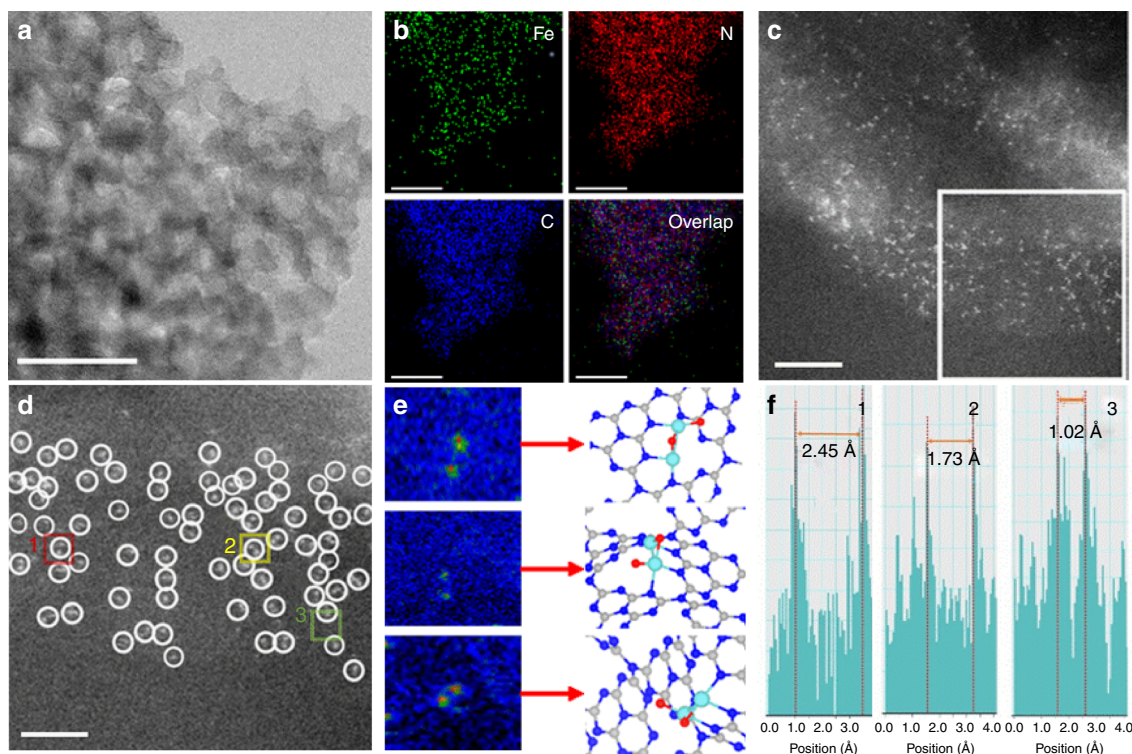


Fig. 1 Characterization of Fe₂/mpg-C₃N₄ clusters. **a** HAADF-STEM images of Fe₂/mpg-C₃N₄. Scale bar, 50 nm. **b** Corresponding element maps showing distributions of Fe (green), N (red), and C (blue), respectively. Scale bar, 50 nm. **c** AC HAADF-STEM images of Fe₂/mpg-C₃N₄. Scale bar, 2 nm. **d** Magnified AC HAADF-STEM images of Fe₂/mpg-C₃N₄. Scale bar, 1 nm. **e**, **f** Intensity profiles obtained in areas 1, 2, and 3

by the HAADF-STEM image (Fig. 1a) and the corresponding energy dispersive X-ray (EDX) mapping analysis (Fig. 1b). The AC HAADF-STEM image (Fig. 1c) with atomic resolution further elucidates the characteristic of Fe atoms, where one can see the small bright dots homogeneously distributed on the mpg-C₃N₄ substrate. Due to the remarkable difference in Z-contrast between Fe and N/C³⁰, the small bright dots are determined to be Fe atoms. Furthermore, in the magnified AC HAADF-STEM image (Fig. 1d), a large proportion of isolated metallic diatoms appears in the regions tagged by white circles, confirming the formation of diatomic Fe₂ clusters. Since the AC HAADF-STEM image represents a two-dimensional projection along the incident beam direction, the detailed features of Fe₂ clusters are different from each other depending on their orientations in three dimensions³¹. For example, a group of bright double dots is consistent with a parallel Fe₂ structure, whereas a single bright dot corresponds to a Fe₂ dimer that is aligned with the projection. The statistical analysis on 100 pairs of Fe₂ dimers shows that the projected Fe–Fe distance between adjacent bright dots varies from 1.20 to 2.45 Å (Supplementary Figure 5). The largest distance, as shown in the intensity profiles (Fig. 1e, f), is consistent with the bond length of a Fe₂ dimer. When the support is replaced by graphene oxide, the Fe₂ clusters agglomerated to Fe nanoparticles (Supplementary Figures 6, 7) during the process of thermal decomposition. It is due to a lack of N atoms that can anchor the Fe₂ clusters. To further illustrate the Fe₂ site, we reduced the loading amount of Fe₂. The AC-STEM images show that the Fe atoms in the spherical electron microscope were still present as Fe₂ clusters, further indicating that the Fe₂ clusters did not decompose into single atoms during the synthetic process (Supplementary Figure 8). We also performed TOF-SIMS characterization of the samples. The data show that there is only Fe₂, but no larger Fe

clusters, such as Fe₃ or Fe₄, indicating that the Fe₂ clusters did not agglomerate (Supplementary Figures 9, 10). The above results demonstrate the importance of the mpg-C₃N₄ support in the synthesis of the Fe₂ catalysts.

XAFS spectroscopy was utilized to probe detailed structure information such as the coordination environment³². Figure 2a shows the Fe k-edge X-ray absorption near-edge structure (XANES) spectra of the Fe₂/mpg-C₃N₄ sample compared with Fe foil and Fe₂O₃ as references. The absorption edge of Fe₂/mpg-C₃N₄ is located between that of Fe foil and Fe₂O₃, suggesting that the Fe atoms carry positive charges and are partially oxidized. The Fourier-transformed (FT) k³-weighted EXAFS spectrum of the Fe₂ precursor is shown in Supplementary Figure 11. Here, a peak at a high R value (ca. 2.50 Å) corresponds to the Fe–Fe coordination path. The other two peaks, at low R values (ca. 1.82 and 2.14 Å), are assigned to the ligands of the Fe₂ precursor. Interestingly, these two peaks disappeared in the spectra of the Fe₂/mpg-C₃N₄ samples (Fig. 2b, c), meaning that the ligands had been completely removed. Figure 2b shows the FT k³-weighted EXAFS spectrum of Fe₂/mpg-C₃N₄. At the FT curve of Fe₂/mpg-C₃N₄, a strong peak is located at ca. 1.53 Å, indicating that the sample is mainly comprised of the Fe–N/O coordination path. Interestingly, a secondary peak, which cannot be ignored at high R value (ca. 2.27 Å), was found in the spectrum of the Fe₂/mpg-C₃N₄ sample. It reveals that some Fe–Fe path should also be accounted for as the surrounding coordination of metal centers. According to the EXAFS fitting results summarized in Fig. 2c, d, Supplementary Table 1, and Supplementary Figures 12–16, the average coordination numbers of Fe–N/O and Fe–Fe are 3.8 and 1.2, respectively. In order to further identify the local structure of Fe₂/mpg-C₃N₄, XANES and EXAFS simulations, which are very sensitive to the 3D arrangement of atoms around the photo-

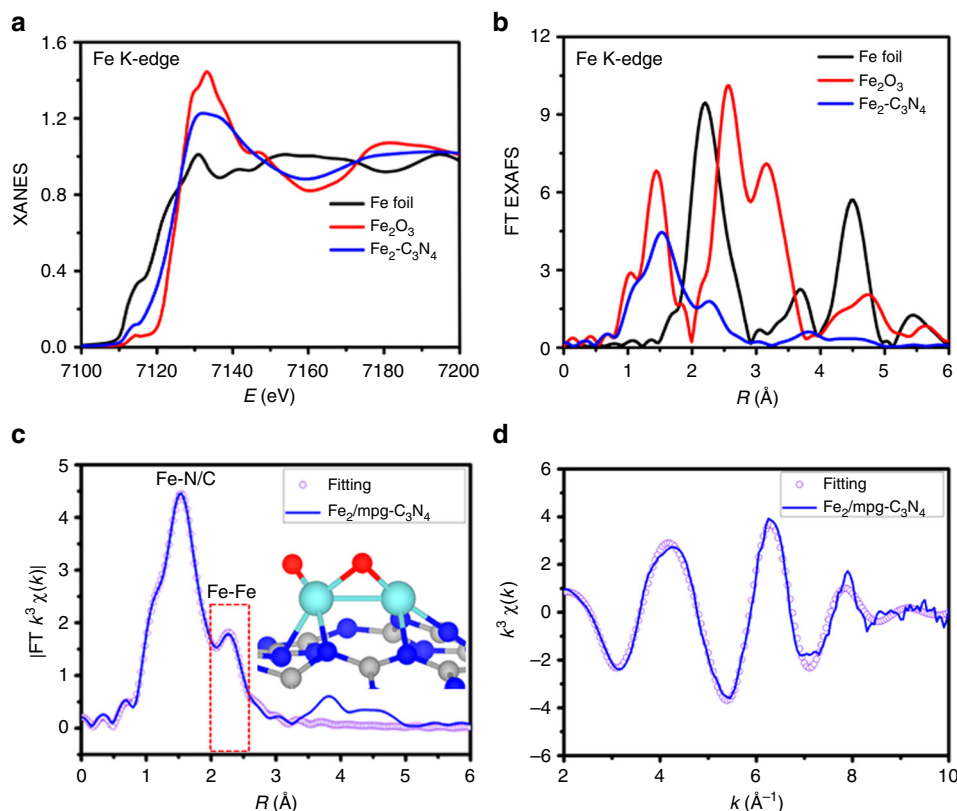


Fig. 2 X-ray absorption analysis of Fe K-edge. **a** XANES spectra at the Fe k-edge of Fe₂/mpg-C₃N₄, Fe₂O₃, and Fe foil. **b** Fourier transform (FT) at the Fe k-edge of Fe₂/mpg-C₃N₄, Fe₂O₃, and Fe foil. **c**, **d** Corresponding fits of the EXAFS spectrum of Fe₂/mpg-C₃N₄ at R space and k space, respectively. The inset of **c** is the schematic model of Fe₂/mpg-C₃N₄ (Fe cyan, O red, N blue, and C gray)

absorber, were carried out at the Fe K-edge. Supplementary Figures 16 and 18 show that the simulated XANES and EXAFS spectrum based on our model agrees well with the experimental results, indicating that this structure is the most likely actual structure. A series of other possible structures were also considered, but the comparison between the simulated spectra and the experimental EXAFS and XANES results is quite unsatisfactory (Supplementary Figures 17 and 19), confirming this structure is the most likely actual structure. Combining the EXAFS fitting and the XANES simulations, the atomic structure of the $\text{Fe}_2/\text{mpg-C}_3\text{N}_4$ sample can be revealed. The structure of $\text{Fe}_2/\text{mpg-C}_3\text{N}_4$ was further identified by first-principles calculations (Fig. 2c, insets and Supplementary Figure 20). Here, Fe atoms are anchored by two N atoms in the graphitic carbon nitride framework. The two Fe atoms are slightly oxidized, connecting with two and one O atoms, respectively. The Fe–Fe bond length was calculated to be 2.40 Å, while it is around 2.2 Å without the presence of O atoms. Bader charge analysis revealed that the two Fe atoms possess positive charges of 1.32 and 1.00, respectively. The information based on DFT calculations agrees very well with results from the XAFS spectrum.

Epoxidation of *trans*-stilbene to *trans*-stilbene oxide. We next investigated the catalytic properties of the as-prepared $\text{Fe}_2/\text{mpg-C}_3\text{N}_4$ sample for epoxidation reactions. We chose *trans*-stilbene as the alkene reactant because of its non-volatility as well as the product stability for a reliable determination of conversion, yield, and selectivity using gas chromatography. Using molecular O_2 as the oxidant and without any additives, the $\text{Fe}_2/\text{mpg-C}_3\text{N}_4$ sample shows unique and superior catalytic performance toward the epoxidation.

As shown in Fig. 3a, we achieved conversion of 91% and selectivity of 93% after 24 h. It is one of the best results for the

epoxidation of *trans*-stilbene to *trans*-stilbene oxide using Fe-based catalysts, employing O_2 as the oxidant without any additive. When bare $\text{mpg-C}_3\text{N}_4$, iron porphyrin, or Fe nanoparticle (ca. 3 nm)/ $\text{mpg-C}_3\text{N}_4$ were used (Supplementary Figures 21, 22), the *trans*-stilbene oxide product was almost undetectable under the same condition, uncovering the unique performance of the diatomic clusters. Single-atom catalysts have attracted much interest because of their remarkable catalytic activity, selectivity, and 100% atom utilization^{33–36}. To further demonstrate the unique performance of $\text{Fe}_2/\text{mpg-C}_3\text{N}_4$, we synthesized the single-atom $\text{Fe}_1/\text{mpg-C}_3\text{N}_4$ sample for comparison. HAADF-STEM, AC HAADF-STEM, and XAFS (Supplementary Figures 23, 24) have confirmed that the as-prepared material contains only single atoms of Fe. When such sample was used, only trace amounts of *trans*-stilbene oxide product were obtained, confirming the unique and superior performance of the diatomic clusters. The performance of the Fe_2 clusters is also compared with that of other known catalysts. Noble metal nanoparticles (such as Ru, Rh, Pd, Au, and Pt) have been demonstrated to be good catalysts for epoxidation^{37,38}. Herein, we synthesized a series of noble metal nanoparticles (Supplementary Figures 25–29). Supplementary Table 2 shows that the activity of $\text{Fe}_2/\text{mpg-C}_3\text{N}_4$ is much better than all the metal nanoparticles. We then collected the $\text{Fe}_2/\text{mpg-C}_3\text{N}_4$ catalyst after the reaction and reused it in the next round of epoxidation reaction. After 15 cycles, the $\text{Fe}_2/\text{mpg-C}_3\text{N}_4$ sample still maintains its pore structure and exhibits robust recycling capability with well-retained activity and selectivity (Fig. 3b). The unchanged structures as fresh samples identified by HAADF-STEM and AC HAADF-STEM images further corroborate the stability of the catalyst (Supplementary Figure 30).

First-principles calculations were performed to explore the underlying reasons for the unique catalytic properties of $\text{Fe}_2/\text{mpg-C}_3\text{N}_4$. In Fig. 3c, the energy profile for the epoxidation of

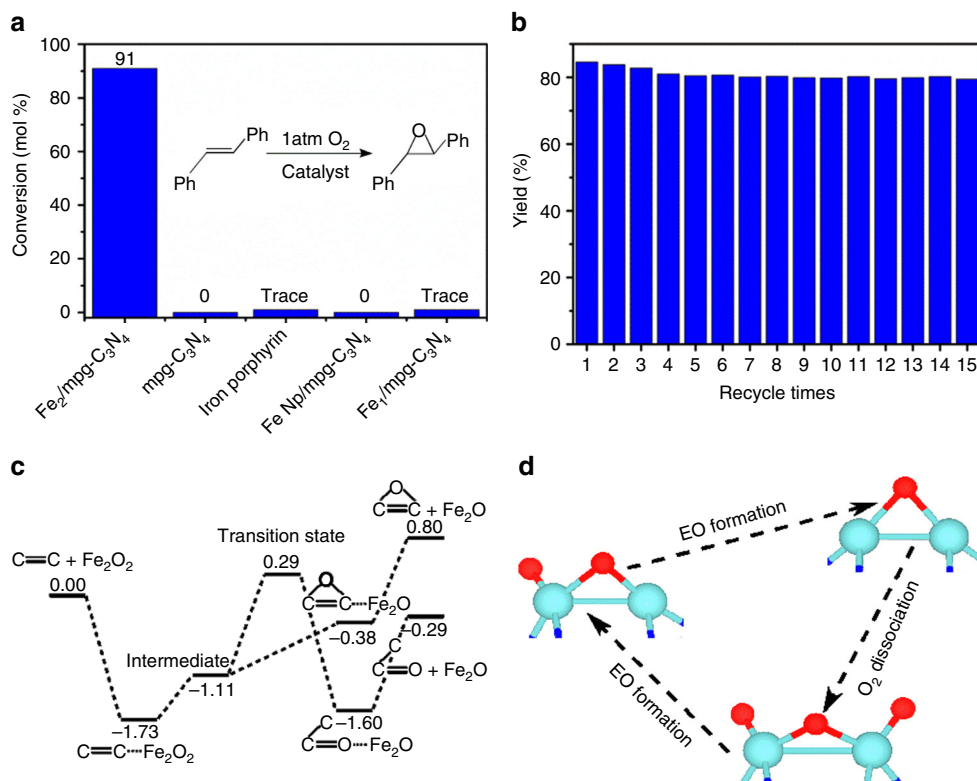


Fig. 3 Epoxidation of *trans*-stilbene. **a** Catalytic epoxidation of *trans*-stilbene using different catalysts. **b** Recycle of $\text{Fe}_2/\text{mpg-C}_3\text{N}_4$ for catalytic epoxidation of *trans*-stilbene. **c** Energy profile (unit: eV) for the *trans*-stilbene epoxidation at the Fe_2O_2 site. **d** Consumption and regeneration of the active one-coordinated oxygen species

trans-stilbene at the Fe₂O₂ site is shown. We found that the alkene molecule first approaches the Fe₂/mpg-C₃N₄ catalyst via a non-planar configuration, where van der Waals interactions play an important role in the adsorption. Then, the molecule connects to the one-coordinated oxygen atom through one of the two carbon atoms in the C=C double bond, bringing about an intermediate state (Supplementary Figure 31) that controls the selectivity of alkene epoxidation^{39–41}. After that, the other carbon atom is bonded to the one-coordinated oxygen atom, leading to the formation of the epoxidized product. Such process merely needs to overcome an energy increase of 0.73 eV. It is worth noting that the value is much lower than the energy barrier of 1.40 eV, which corresponds to a competitive pathway toward the formation of combustion products^{39–41}. In the above process, only the one-coordinated oxygen atoms are active and play an important role, whereas the two-coordinated ones behave as bystanders. It is interesting to find that once one active oxygen species is consumed in the alkene epoxidation, two more one-coordinated oxygen atoms can be generated via O₂ dissociation at the Fe₂O site (Supplementary Figure 32). The O₂ dissociation involves the formation of a highly activated molecular precursor and a significant energy release of 3.32 eV, which makes it a very facile process. In Fig. 3d, we schematically present the consumption and regeneration of the active oxygen species. Here, the catalytic activity and selectivity of the produced Fe₂O₃ are quite similar as those of Fe₂O₂, with the corresponding epoxidation profile shown in Supplementary Figure 33.

The striking difference in the catalytic activity of Fe₂/mpg-C₃N₄, Fe nanoparticles, and iron porphyrin is attributed to the variation of the interaction strength between O₂ molecules and the corresponding Fe species. For a good catalytic performance, such interaction should be neither too strong nor too weak^{42,43}.

On Fe nanoparticles, the interaction between their surface layers and the oxygen reactants is very strong^{44,45}, producing tightly bound oxygen atoms that can hardly participate in the epoxidation reaction. Regarding the iron porphyrin, by contrast, the interaction of O₂ with the embedded single Fe atom is too weak and only molecular adsorption is possible (Supplementary Figure 34). The bond length of 1.30 Å in the adsorbate, compared with that of 1.24 Å in isolated O₂, demonstrates that such molecule has not been well activated. Thus, neither Fe nanoparticles nor iron porphyrin can generate the active oxygen species as in the case of the Fe₂/mpg-C₃N₄ catalyst.

Synthesis and characterization of other TM₂/mpg-C₃N₄ samples. Some other transition-metal (for example, TM = Pd, Ir) clusters were produced using the same scheme, which demonstrates the general applicability of the approach for synthesizing diatomic clusters (Supplementary Figures 35–36). In the AC HAADF-STEM images (Fig. 4c, f, inset), a large proportion of bright double dots was observed in the regions tagged by white circles, indicating the existence of isolated metallic dimers in TM₂/mpg-C₃N₄. EXAFS spectrum was further used to confirm the as-obtained TM₂/mpg-C₃N₄ samples (Fig. 4a–f, Supplementary Figures 37–42, and Supplementary Table 3). In the FT k³-weighted EXAFS spectrum shown in Fig. 4b, e, the first strong FT curves of TM k-edge in TM₂/mpg-C₃N₄ show peaks at 1.45 Å for Pd₂/mpg-C₃N₄ and 1.63 Å for Ir₂/mpg-C₃N₄ (before phase shift correction), indicating that TM₂/mpg-C₃N₄ is mainly comprised of the TM–N coordination path. Similarly, a secondary peak at high R value (2.35 Å for Pd₂/mpg-C₃N₄ and 2.49 Å for Ir₂/mpg-C₃N₄) was found, which demonstrates that metal–metal path should also be accounted for as in the case of Fe₂/mpg-C₃N₄.

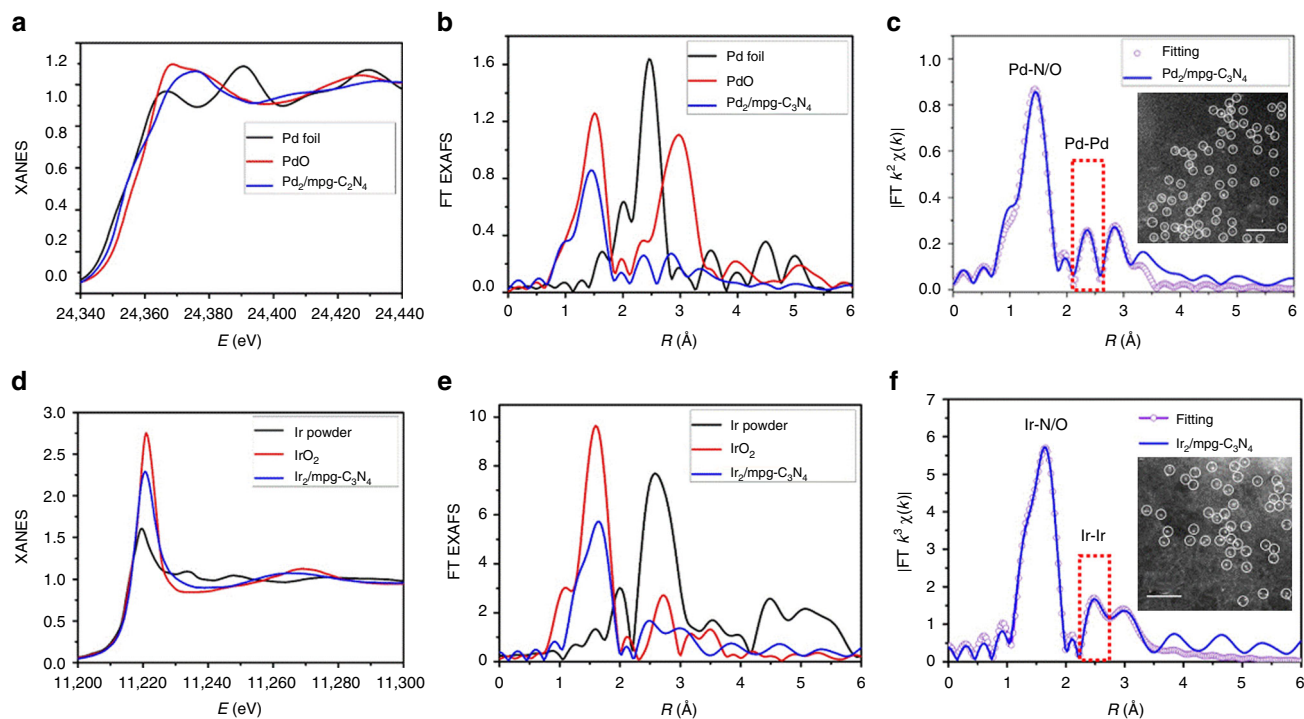


Fig. 4 Characterization of other TM₂/mpg-C₃N₄ clusters. **a** XANES spectra at the Pd k-edge of Pd₂/mpg-C₃N₄, PdO, and Pd foil. **b** Fourier transform (FT) at the Pd k-edge of Pd₂/mpg-C₃N₄, PdO, and Pd foil. **c** Corresponding fits of the EXAFS spectrum of Pd₂/mpg-C₃N₄ at R space. The inset of (**c**) is the AC HAADF-STEM of Pd₂/mpg-C₃N₄, scale bar, 1 nm. **d** XANES spectra at the Ir L₃-edge of Ir₂/mpg-C₃N₄, IrO₂, and Ir powder. **e** Fourier transform at the Ir L₃-edge of Ir₂/mpg-C₃N₄, IrO₂, and Ir powder. **f** Corresponding fits of the EXAFS spectrum of Ir₂/mpg-C₃N₄ at R space. The inset of (**f**) is the AC HAADF-STEM of Ir₂/mpg-C₃N₄, scale bar, 1 nm

Discussion

In summary, we have developed a “precursor-preselected” wet-chemistry strategy to synthesize Fe₂ clusters supported on mpg-C₃N₄, whose structures are identified using AC-STEM, XAFS, and first-principles calculations. By employing molecular oxygen as the oxidant and in the absence of aldehyde as co-reagent, the as-prepared Fe₂/mpg-C₃N₄ sample exhibits unique and superior catalytic performance toward alkene epoxidation. By contrast, iron porphyrin, single-atom Fe, and small Fe nanoparticles are nearly reactively inert. First-principles calculations reveal that the unique reactivity of Fe₂ comes from the formation of active oxygen species. Our scheme can be applied toward producing other diatomic clusters and establishes a substantial foundation for further studies of atomically precise sub-nano catalysts.

Methods

Preparation of mpg-C₃N₄. A method was used according to a previous report with a tiny modification. Aliquot of 5 g of cyanamide and 12.5 g of colloidal silica Ludox HS-40 are mixed together until complete dissolution of cyanamide. The mixture was heated in an oil bath at 100 °C upon stirring for ca. 3 h until removal of water and formation of a white solid. The powder was then grounded in a mortar, transferred into a crucible, and heated under air at 2.3 °C min⁻¹ (4 h) up to 550 °C and then treated at 550 °C for 4 h. The as-obtained yellow powder was grounded in a mortar and then treated under stirring for 2 days in an NH₄FH₂ 4 mol L⁻¹ solution. The dispersion was then filtered, the precipitate washed with distilled water and ethanol. After filtering, the yellow compound is dried under vacuum at 100 °C overnight.

Synthesis of Fe₂/mpg-C₃N₄. In a typical synthesis of Fe₂/mpg-C₃N₄, 5 mg bis(dicarbonylcyclopentadienyliron) (Fe₂O₄C₁₄H₁₀) and mpg-C₃N₄ (500 mg) were dissolved in the DMF (100 mL) under stirring at room temperature for 24 h. The product was separated by centrifugation at 10,000 rpm for 5 min and washed subsequently with DMF for once, then washed with methanol for once and finally dried under vacuum at room temperature. The as-prepared powder was transferred into a ceramic broth and then placed into a tube furnace maintaining 300 °C for 2 h under flowing mixture of 5% H₂/Ar atmosphere with a heating rate of 5 °C min⁻¹. When the temperature is above 250 °C, thermogravimetric analysis (TGA) shows a weight loss of 30.8 wt%, similar to the theoretical loss of 31.5 wt% according to the formula when the ligand is removed completely (Supplementary Figure 43). Therefore, we chose 300 °C to thoroughly remove the organic ligands. The Fe loading is 0.15% determined by ICP-AES analysis.

XAFS measurements and analysis. The X-ray absorption fine structure spectra data (Fe k-edge and Ir L₃-edge) were collected at 1W1B station in Beijing Synchrotron Radiation Facility (BSRF, operated at 2.5 GeV with a maximum current of 250 mA). The X-ray absorption fine structure spectra data (Pd k-edge) were collected at 14W1 station in Shanghai Synchrotron Radiation Facility (SSRF, 3.5 GeV, 250 mA). The data were collected in fluorescence excitation mode using a Lytle detector. All samples were pelletized as disks of 13 mm diameter with 1 mm thickness using graphite powder as a binder. Using the ATHENA module in the IFEFFIT packages, we processed the acquired EXAFS data following the standard procedures. After the subtraction of the post-edge background and normalization, the EXAFS spectra was obtained. Then, the $\chi(k)$ data were transformed to R space. Using the ARTEMIS module, we obtained the quantitative structural parameters via a least-squares curve parameter fitting method.

Typical procedure for the epoxidation of trans-stilbene. In this typical reaction, trans-stilbene (90.12 mg, 0.50 mmol), Fe₂/mpg-C₃N₄, iron porphyrin, or Fe nanoparticle/mpg-C₃N₄ (ca. 3 nm) (0.50 μ mol Fe) and DMAC (5 mL) were mixed in a 20 mL of Schlenk tube. Then, we used an oil pump to remove the air in the tube. An O₂ balloon was used to blow about 1 atm O₂. Finally, the reaction vessel was heated in a silicon oil bath at 90 °C. The mixture was stirred at this temperature for 24 h. The products were identified by gas chromatography (GC).

Computational details. The mpg-C₃N₄ framework was simulated by a graphitic carbon nitride (g-C₃N₄) monolayer that exhibits a corrugated non-planar configuration. We adopted its optimized lattice constant of 6.937 Å and constructed a hexagonal 2 × 2 unit cell accordingly (Supplementary Figure 16). An Fe₂ dimer with different numbers of O atoms was deposited at various locations on the g-C₃N₄ substrate, in order to carry out an extensive structural exploration.

Spin-polarized density functional theory calculations were performed based on the projector-augmented-wave (PAW) approach⁴⁶, utilizing the Vienna ab initio simulation package (VASP)^{47,48}. The energy cutoff of the plane-waves basis set to 500 eV. The exchange-correlation interactions were described by the optPBE-vdW functional^{49,50}. The first Brillouin zone was sampled using a 3 × 3 × 1 Monkhorst-Pack grid⁵¹. Structural relaxations were performed until the maximum

residual force on each atom was <0.02 eV Å⁻¹. The transition state was located using the climbing image nudged elastic band method⁵² with a force criterion of 0.05 eV Å⁻¹. A dipole correction to the total energies was applied along the vertical direction. Bader charge analysis was carried out with core charges included in the partitions⁵³. All structures were visualized using the program VESTA⁵⁴.

Data availability. The data supporting this study are available from the authors on reasonable request.

Received: 11 October 2017 Accepted: 24 May 2018

Published online: 15 June 2018

References

- Kaden, W. E., Wu, T., Kunkel, W. A. & Anderson, S. L. Electronic structure controls reactivity of size-selected Pd clusters adsorbed on TiO₂ surfaces. *Science* **326**, 826–829 (2009).
- Vajda, S. et al. Subnanometre platinum clusters as highly active and selective catalysts for the oxidative dehydrogenation of propane. *Nat. Mater.* **8**, 213–216 (2009).
- Lopez-Acevedo, O., Kacprzak, K. A., Akola, J. & Hakkinen, H. Quantum size effects in ambient CO oxidation catalysed by ligand-protected gold clusters. *Nat. Chem.* **2**, 329–334 (2010).
- Corma, A. et al. Exceptional oxidation activity with size-controlled supported gold clusters of low atomcity. *Nat. Chem.* **5**, 775–781 (2013).
- Nesselberger, M. et al. The effect of particle proximity on the oxygen reduction rate of size-selected platinum clusters. *Nat. Mater.* **12**, 919–924 (2013).
- Guan, H. et al. Catalytically active Rh sub-nanoclusters on TiO₂ for CO oxidation at cryogenic temperatures. *Angew. Chem. Int. Ed.* **55**, 2820–2824 (2016).
- Luo, Z., Castleman, A. W. Jr. & Khanna, S. N. Reactivity of metal clusters. *Chem. Rev.* **116**, 14456–14492 (2016).
- Liu, Y. et al. Coupling sub-nanometric copper clusters with quasi-amorphous cobalt sulfide yields efficient and robust electrocatalysts for water splitting reaction. *Adv. Mater.* **29**, 1606200 (2017).
- Chen, Z., Li, J., Li, S. & Wang, L.-W. Glass-like energy and property landscape of Pt nanoclusters. *Nano Res.* **10**, 2721–2731 (2017).
- Turner, M. et al. Selective oxidation with dioxygen by gold nanoparticle catalysts derived from 55-atom clusters. *Nature* **454**, 981–985 (2008).
- Lei, Y. et al. Increased silver activity for direct propylene epoxidation via subnanometer size effects. *Science* **328**, 224–228 (2010).
- Tyo, E. C. & Vajda, S. Catalysis by clusters with precise numbers of atoms. *Nat. Nanotechnol.* **10**, 577–588 (2015).
- Crampton, A. S. et al. Controlling ethylene hydrogenation reactivity on Pt₁₃ clusters by varying the stoichiometry of the amorphous silica support. *Angew. Chem. Int. Ed.* **55**, 8953–8957 (2016).
- Li, X. N., Zhang, H. M., Yuan, Z. & He, S. G. A nine-atom rhodium-aluminum oxide cluster oxidizes five carbon monoxide molecules. *Nat. Commun.* **7**, 11404 (2016).
- Fortea-Perez, F. R. et al. The MOF-driven synthesis of supported palladium clusters with catalytic activity for carbene-mediated chemistry. *Nat. Mater.* **16**, 760–766 (2017).
- Ji, S. et al. Confined pyrolysis within metal-organic frameworks to form uniform Ru₃ clusters for efficient oxidation of alcohols. *J. Am. Chem. Soc.* **139**, 9795–9798 (2017).
- Hakkinen, H. The gold-sulfur interface at the nanoscale. *Nat. Chem.* **4**, 443–455 (2012). 1352.
- Lv, C. et al. Pd₃ cluster catalysis: compelling evidence from in operando spectroscopic, kinetic, and density functional theory studies. *Nano Res.* **9**, 2544–2550 (2016).
- Kwak, K. et al. A molecule-like PtAu₂(SC₆H₁₃)₁₈ nanocluster as an electrocatalyst for hydrogen production. *Nat. Commun.* **8**, 14723 (2017).
- Ortalan, V., Uzun, A., Gates, B. C. & Browning, N. D. Direct imaging of single metal atoms and clusters in the pores of dealuminated HY zeolite. *Nat. Nanotechnol.* **5**, 506–510 (2010).
- Uzun, A., Dixon, D. A. & Gates, B. C. Prototype supported metal cluster catalysts: Ir₄ and Ir₆. *ChemCatChem* **3**, 95–107 (2011).
- Bitterlich, B. et al. Development of a general and efficient iron-catalyzed epoxidation with hydrogen peroxide as oxidant. *Chem. Asian J.* **2**, 521–529 (2007).
- Chen, L., Yang, Y., Guo, Z. & Jiang, D. Highly efficient activation of molecular oxygen with nanoporous metalloporphyrin frameworks in heterogeneous systems. *Adv. Mater.* **23**, 3149–3154 (2011).
- Cusso, O., Garcia-Bosch, I., Ribas, X., Lloret-Fillol, J. & Costas, M. Asymmetric epoxidation with H₂O₂ by manipulating the electronic properties of non-heme iron catalysts. *J. Am. Chem. Soc.* **135**, 14871–14878 (2013).

25. Neumann, R. & Dahan, M. Aruthenium-substituted polyoxometalate as an inorganic dioxygenase for activation of molecular oxygen. *Nature* **388**, 353–355 (1997).
26. Nishiyama, Y., Nakagawa, Y. & Mizuno, N. High turnover numbers for the catalytic selective epoxidation of alkenes with 1 atm of molecular oxygen. *Angew. Chem. Int. Ed.* **40**, 3639–3641 (2001).
27. Goettmann, F., Fischer, A., Antonietti, M. & Thomas, A. Chemical synthesis of mesoporous carbon nitrides using hard templates and their use as a metal-free catalyst for Friedel-Crafts reaction of benzene. *Angew. Chem. Int. Ed.* **45**, 4467–4471 (2006).
28. Yan, S. C., Li, Z. S. & Zou, Z. G. Photodegradation performance of g-C₃N₄ fabricated by directly heating melamine. *Langmuir* **25**, 10397–10401 (2009).
29. Xiang, Q., Yu, J. & Jaroniec, M. Preparation and enhanced visible-light photocatalytic H₂-production activity of graphene/C₃N₄ composites. *J. Phys. Chem. C* **115**, 7355–7363 (2011).
30. Kulkarni, A., Chi, M., Ortalan, V., Browning, N. D. & Gates, B. C. Atomic resolution of the structure of a metal-support interface: triosmium clusters on MgO(110). *Angew. Chem. Int. Ed.* **49**, 10089–10092 (2010).
31. Li, Z. Y. et al. Three-dimensional atomic-scale structure of size-selected gold nanoclusters. *Nature* **451**, 46–48 (2008).
32. Sun, Z., Liu, Q., Yao, T., Yan, W. & Wei, S. X-ray absorption fine structure spectroscopy in nanomaterials. *Sci. China Mater.* **58**, 313–341 (2015).
33. Qiao, B. et al. Single-atom catalysis of CO oxidation using Pt₁/FeO_x. *Nat. Chem.* **3**, 634–641 (2011).
34. Liu, J. Catalysis by supported single metal atoms. *ACS Catal.* **7**, 34–59 (2017).
35. Zhang, M. et al. Metal (Hydr)oxides@polymer core-shell strategy to metal single-atom materials. *J. Am. Chem. Soc.* **139**, 10976–10979 (2017).
36. Zhu, C., Fu, S., Shi, Q., Du, D. & Lin, Y. Single-atom electrocatalysts. *Angew. Chem. Int. Ed.* **56**, 13944–13960 (2017).
37. Noh, J.-H., Patala, R. & Meijboom, R. Catalytic evaluation of dendrimer and reverse microemulsion template Pd and Pt nanoparticles for the selective oxidation of styrene using TBHP. *Appl. Catal. A Gen.* **514**, 253–266 (2016).
38. Liu, B. et al. Au–carbon electronic interaction mediated selective oxidation of styrene. *ACS Catal.* **7**, 3483–3488 (2017).
39. Linic, S. & Barteau, M. A. Formation of a stable surface oxametallacycle that produces ethylene oxide. *J. Am. Chem. Soc.* **124**, 310–317 (2002).
40. Linic, S. Construction of a reaction coordinate and a microkinetic model for ethylene epoxidation on silver from DFT calculations and surface science experiments. *J. Catal.* **214**, 200–212 (2003).
41. Linic, S. & Barteau, M. A. Control of ethylene epoxidation selectivity by surface oxametallacycles. *J. Am. Chem. Soc.* **125**, 4034–4035 (2003).
42. Nørskov, J. K., Bligaard, T., Rossmeisl, J. & Christensen, C. H. Towards the computational design of solid catalysts. *Nat. Chem.* **1**, 37–46 (2009).
43. Nørskov, J. K., Studt, F., Abild-Pedersen, F. & Bligaard, T. *Fundamental Concepts in Heterogeneous Catalysis* (John Wiley & Sons, Inc., New Jersey, 2014). **3**.
44. Linderoth, S., Mørup, S. & Bentzon, M. D. Oxidation of nanometer-sized iron particles. *J. Mater. Sci.* **30**, 3142–3148 (1995).
45. Giri, S., Ganguli, S. & Bhattacharya, M. Surface oxidation of iron nanoparticles. *Appl. Surf. Sci.* **182**, 345–349 (2001).
46. Blöchl, P. E. Projector augmented-wave method. *Phys. Rev. B* **50**, 17953–17979 (1994).
47. Kresse, G. & Furthmüller, J. Efficiency of ab-initio total energy calculations for metals and semiconductors using a plane-wave basis set. *Comput. Mater. Sci.* **6**, 15–50 (1996).
48. Kresse, G. & Furthmüller, J. Efficient iterative schemes for ab initio total-energy calculations using a plane-wave basis set. *Phys. Rev. B* **54**, 11169–11186 (1996).
49. Dion, M., Rydberg, H., Schröder, E., Langreth, D. C. & Lundqvist, B. I. Van der Waals density functional for general geometries. *Phys. Rev. Lett.* **92**, 246401 (2004).
50. Klimeš, J., Bowler, D. R. & Michaelides, A. Chemical accuracy for the van der Waals density functional. *J. Phys. Condens. Matter* **22**, 022201 (2010).
51. Monkhorst, H. J. & Pack, J. D. Special points for Brillouin-zone integrations. *Phys. Rev. B* **13**, 5188–5192 (1976).
52. Henkelman, G., Uberuaga, B. P. & Jónsson, H. A climbing image nudged elastic band method for finding saddle points and minimum energy paths. *J. Chem. Phys.* **113**, 9901–9904 (2000).
53. Tang, W., Sanville, E. & Henkelman, G. A grid-based Bader analysis algorithm without lattice bias. *J. Phys. Condens. Matter* **21**, 084204 (2009).
54. Momma, K. & Izumi, F. VESTA 3 for three-dimensional visualization of crystal, volumetric and morphology data. *J. Appl. Cryst.* **44**, 1272–1276 (2011).

Acknowledgements

This work was supported by China Ministry of Science and Technology under Contract of 2016YFA (0202801), the National Natural Science Foundation of China (21521091, 21390393, U1463202, 21471089, and 21671117). Q.F. and C.D. acknowledge support from the German Research Foundation (DFG) and the European Union's Horizon 2020 research and innovation programme, Grant Agreement No. 676580 through the Center of Excellence NOMAD. Q.F. thanks supports from the Fundamental Research Funds of Shandong University (2018TB006). This work made use of the resources support of National Synchrotron Radiation Laboratory in Beijing and Shanghai.

Author contributions

D.W. and Y.L. conceived and designed the research project. S.T. conducted and designed the experiments, analyzed the data, and wrote the paper. Q.F. and C.D. conducted the first-principles simulations and contributed to the writing of the paper. W.C. completed the XAFS characterization and corresponding data analysis. J.D. analyzed XANES data. Q.F., C.C., and Q.P. helped to analyze the data. L.G., R.Y., and J.L. provided spherical-aberration-corrected TEM techniques. Z.C. and J.Z. assisted to carry out the catalytic experiments. W.C. conducted HAAD-STEM. All authors contributed to the preparation of the manuscript.

Additional information

Supplementary Information accompanies this paper at <https://doi.org/10.1038/s41467-018-04845-x>.

Competing interests: The authors declare no competing interests.

Reprints and permission information is available online at <http://npg.nature.com/reprintsandpermissions/>

Publisher's note: Springer Nature remains neutral with regard to jurisdictional claims in published maps and institutional affiliations.



Open Access This article is licensed under a Creative Commons Attribution 4.0 International License, which permits use, sharing, adaptation, distribution and reproduction in any medium or format, as long as you give appropriate credit to the original author(s) and the source, provide a link to the Creative Commons license, and indicate if changes were made. The images or other third party material in this article are included in the article's Creative Commons license, unless indicated otherwise in a credit line to the material. If material is not included in the article's Creative Commons license and your intended use is not permitted by statutory regulation or exceeds the permitted use, you will need to obtain permission directly from the copyright holder. To view a copy of this license, visit <http://creativecommons.org/licenses/by/4.0/>.

© The Author(s) 2018